



Article

Soil-Moisture Estimation Based on Multiple-Source Remote-Sensing Images

Tianhao Mu ¹, Guiwei Liu ², Xiguang Yang ^{1,3,*}  and Ying Yu ^{1,3} ¹ School of Forestry, Northeast Forestry University, Harbin 150040, China² China Railway Design Corporation, Tianjin 300251, China³ Key Laboratory of Sustainable Forest Ecosystem Management-Ministry of Education, Northeast Forestry University, Harbin 150040, China

* Correspondence: yangxiguang@nefu.edu.cn

Abstract: Soil moisture plays a significant role in the global hydrological cycle, which is an important component of soil parameterization. Remote sensing is one of the most important methods used to estimate soil moisture. In this study, we developed a new nonlinear Erf-BP neural network method to establish a soil-moisture-content-estimation model with integrated multiple-resource remote-sensing data from high-resolution, hyperspectral and microwave sensors. Next, we compared the result with the single-resource remote-sensing data for SMC (soil-moisture content) estimation models by using the linear-fitting method. The results showed that the soil-moisture estimation model offers better accuracy by using multiple-resource remote-sensing data. Furthermore, the SMC predicted the results by using the new Erf-BP neural network with multiple-resource remote-sensing data and a good overall correlation coefficient of 0.6838. Compared with the linear model's estimation results, the accuracy of the SMC estimation using the Erf-BP method was increased, and the RMSE decreased from 0.017 g/g to 0.0146 g/g, a decrease of 16.44%. These results also indicate that the improved algorithm of the Erf-BP artificial neural network has better fitting results and precision. This research provides a reference for multiple-resource remote-sensing data for soil-moisture estimation.

Keywords: soil moisture; Erf-BP neural network; multiple-resource remote sensing



Citation: Mu, T.; Liu, G.; Yang, X.; Yu, Y. Soil-Moisture Estimation Based on Multiple-Source Remote-Sensing Images. *Remote Sens.* **2023**, *15*, 139. <https://doi.org/10.3390/rs15010139>

Academic Editors: Hui Lu, Hongquan Wang, Lun Gao and Xiaojun Li

Received: 15 November 2022

Revised: 22 December 2022

Accepted: 23 December 2022

Published: 26 December 2022



Copyright: © 2022 by the authors. Licensee MDPI, Basel, Switzerland. This article is an open access article distributed under the terms and conditions of the Creative Commons Attribution (CC BY) license (<https://creativecommons.org/licenses/by/4.0/>).

1. Introduction

Soil moisture is a key state variable of the three-phase system of soils, and has significant importance for the Earth and for environmental-science applications [1]. Soil moisture is an important characterization of soil water and an important component of soil parameterization [2]. Soil moisture plays a key role in the essential process of water exchange among soil, the atmosphere and water bodies [3]. Soil moisture affects soil respiration, as well as the cycle of soil carbon and even global carbon [4]. Therefore, soil moisture can affect global climate change and even global warming. In addition, surface-soil-moisture content is an important parameter in micrometeorology and hydrology studies [5]. Surface-soil-moisture content also can be an important index of drought monitoring. It has a guiding significance for agricultural production and drought-disaster prevention and reduction [1,6]. Therefore, the study of the acquiring or prediction of soil moisture with high accuracy has certain ecological, economic and social value.

The methods used to determine or predict soil moisture can be divided into two types: the conventional method and the modern method [7]. Generally, the conventional method is the thermo-gravimetric technique and the calcium-carbide technique, in which field sampling and laboratory determination are commonly needed [7,8]. In the thermo-gravimetric technique, soil samples are dried in an oven at 105 °C for 24 h. Next, they are quickly weighed, and their weights are recorded. Finally, the soil-moisture content is obtained by calculating the fraction of the oven-dry weight. The accuracy is ±1% [9]. The time-domain reflectometry (TDR), neutron-scattering-probe method, frequency-domain

reflectometry (FDR), heat-flux technique and resistive method are the most commonly used methods to measure soil moisture [10]. Although conventional methods have many advantages, such as their high accuracy, short duration, simple principle and so on [11], they also have disadvantages, such as their complex sampling processes and a large number of repeated experiments, the limitations of various soil samples for laboratory measuring and so on [12]. The TDR, neutron-scattering-probe method and FDR are expensive and complicated. The heat-flux technique and the resistive method are simple to use and affordable, but they need soil-specific calibration and have high response times [10]. The dielectric technique is only suitable for measuring the moisture of single soils [1,7]. The above methods of soil-moisture-content measurements are based on ground measurements and experiments. At the same time, most of these methods can only monitor specific locations and are inadequate for monitoring the spatial distribution of soil moisture on a large scale [13].

Compared with these conventional methods, remote-sensing technology is one of the most important tools for monitoring and estimating large-scale near-surface soil moisture [14]. Remote-sensing technology has some advantages and has been applied for soil-moisture estimation since the 1970s. Different remote-sensing sensors are utilized to inverse the soil-moisture content. Currently, three main types of remote-sensing sensors are applied to obtain soil-moisture content: optical, thermal, and microwave [15]. The optical remote-sensing method is itself divided into three types: remote-sensing images based on the spatial and spectral resolution, including high spatial resolution, hyperspectral bands (400–2500 nm) and multi-spectral bands (several narrow bands in the visible band and near-infrared band) to analyze the near-surface soil properties [16–19]. In optical remote sensing, the reflectance from 350 nm to 2500 nm was used to estimate the soil moisture [1]. Furthermore, a linear or nonlinear model was established to estimate soil moisture [18,20]. However, the accuracy of the soil-moisture estimation varied depending on the data, the correlation coefficient R varied from 0.89 to 0.95 and the RMSE (root-mean-square error) varied from 0.025 to 0.126 cm^3/cm^3 [16,17,21]. The optical-remote-sensing methods also have some disadvantages, such as the fact that optical-remote-sensing images are affected by weather conditions and the accuracy of soil moisture estimation is affected by vegetation cover on soil surfaces [21].

Bands with wavelengths from approximately 3500 nm to 14,000 nm were used to estimate the soil-moisture content in thermal infrared remote sensing [22]. Furthermore, the determination of land-surface temperature (LST) via evapotranspiration was commonly used to estimate soil moisture with an acceptable level of accuracy ($R^2 = 0.79$) [23]. Furthermore, the soil-moisture index and triangle method are also widely used approaches for soil-moisture estimation by using thermal remote-sensing images [24]. Compared to optical-remote-sensing images, the application of thermal remote sensing for soil-moisture estimation has been limited due to high acquisition costs. With the developments in low-cost remote-sensing platforms, such as unmanned aerial systems (UAVs), high-spatial and temporal-resolution thermal images have become available at a low cost and increased the ability to understand the variability of soil conditions [25].

With the advances in microwave-remote-sensing technology, microwave remote sensing has become an alternative to soil-moisture monitoring. Microwave-remote-sensing technology can extract information by identifying the vast disparity in the dielectric permittivity of water, air and solids [1]. Small changes in the soil-moisture content affect the emissivity and backscattering of microwaves on the soil surface [26]. By analyzing the change in the complex permittivity of the soil, the soil-moisture information can be extracted from microwave remote sensing [27–29]. Therefore, a variety of frequency microwave data, such as P-band [30,31], L-band [32,33], C-band [34,35] and X-band data [36,37] are commonly used to retrieve soil moisture. Microwave remote sensing has a wide range of applications, high stability and good adaptability with high accuracy (RMSE between 0.0395 and 0.0543 cm^3/cm^3) [38,39]. Microwave remote sensing data can also provide a continual large-scale soil-moisture estimation. Some established methodologies for estimating soil

moisture from the Soil Moisture Active Passive (SMAP) and Soil Moisture and Ocean Salinity (SMOS) satellite missions have been published [40,41]. The SMOS and SMAP are the most effective techniques for soil-moisture monitoring on the global scale [1]; global-scale soil moisture in the top 5 cm of soil became detectable through the use of passive or active sensors [42,43]. However, the dielectric properties of the soil phases change according to the soil texture, soil moisture, soil salinity and covered vegetation, which increases the estimation error of the soil moisture from microwave remote sensing [43]. At the same time, microwave remote sensing commonly has a coarse spatial resolution, especially for the SMOS and SMAP; it also increases the uncertainty of the soil-moisture estimation [13,44,45]. Therefore, the integration of different sources of remote-sensing (multi-source remote sensing) data can help to optimize soil-moisture-content estimation [46].

Multi-source remote-sensing technology means space monitoring and image-forming technology, which can integrate different types of remote-sensing data with linear or nonlinear statistical methods, such as optical, thermal infrared and microwave-remote-sensing data [47]. Han et al. (2020) developed a multi-source remote-sensing model with panchromatic-band and thermal-infrared-band remote-sensing data from the Landsat-8 satellite based on the Bayesian maximum-entropy nonlinear statistical method to analyze and predict regional soil-moisture content. Since the model considers influences from the atmosphere, surface conditions and natural radiations, atmospheric, radiation and geometrical corrections were made to the model. The model obtained a perfect effect and offers excellent accuracy, with an RMSE of $0.0423 \text{ cm}^3/\text{cm}^3$ [47]. Wang et al. (2020) analyzed and predicted the soil moisture over wheat farmlands with C-band SAR data from the Sentinel-1 satellite, high-resolution and multispectral optical data from the Sentinel-2 satellite, thermal-infrared and panchromatic remote-sensing data from the Landsat-8 satellite and high-resolution panchromatic and multispectral remote-sensing data from the GF-1 satellite. They combined the WCM (water cloud model, related to vegetation scattering) and the AIEM (advanced integral equation model, related to physics) to establish a soil-moisture linear inversing model and compare the results of various remote-sensing data. The results showed that the estimations of the Sentinel-2 satellite had the best accuracy, with an RMSE of 4.73%, among the four satellites; the others had RMSEs of 6.18%, 5.21% and 6.44%, respectively [48]. These studies and applications are helpful for our studies of soil-moisture estimation, since they use the high-resolution, microwave and full-band hyperspectral remote-sensing data.

In this study, we carried out field-soil-sample collections and field-reflectance measurements. At the same time, we obtained synchronous remote-sensing data, which included the GF-2 high-resolution satellite, GF-3 microwave satellite and GF-5 hyperspectral remote-sensing data. We compared the soil-moisture results by using high-resolution optical remote sensing, hyperspectral remote sensing and microwave remote sensing, and developed a new soil-moisture-estimation method by using a nonlinear neural network model combined with the advantage of multiple-resource remote sensing. To achieve this aim, we carried out in situ samplings and measured the soil moisture and its reflectance. Second, the relationship between the soil moisture and its reflectance of different remote sensors was analyzed. Third, the soil-moisture-estimation models of three different remote sensors were established by using a newly developed back-propagation neural network (BPNN) and the results were compared. Finally, a new soil-moisture-estimation model combining three different sets of remote-sensing data was established by using the BPNN and the accuracy of the improved model was evaluated. This study can provide a reference for soil-moisture estimation by using multiple-resource remote-sensing data.

2. Materials and Data

2.1. Study Area

The research region was located in Xinzhou, Shanxi Province, in the center of China. Xinzhou is located on the Loess Plateau. The region features a temperate continental monsoon climate, and the annual average temperature is between $4.3 \text{ }^\circ\text{C}$ and $9.2 \text{ }^\circ\text{C}$. The

annual precipitation is 345–588 mm. The area of this study region is 30 km × 40 km, forming an area of approximately 1200 km². This region is part of the Xiong’an–Xinzhou Railway works area. The soil samples were collected between 11 May and 14 May 2019. There was no precipitation during data collection. In total, 41 soil samples were collected. The research region and sample sites are shown in Figure 1.

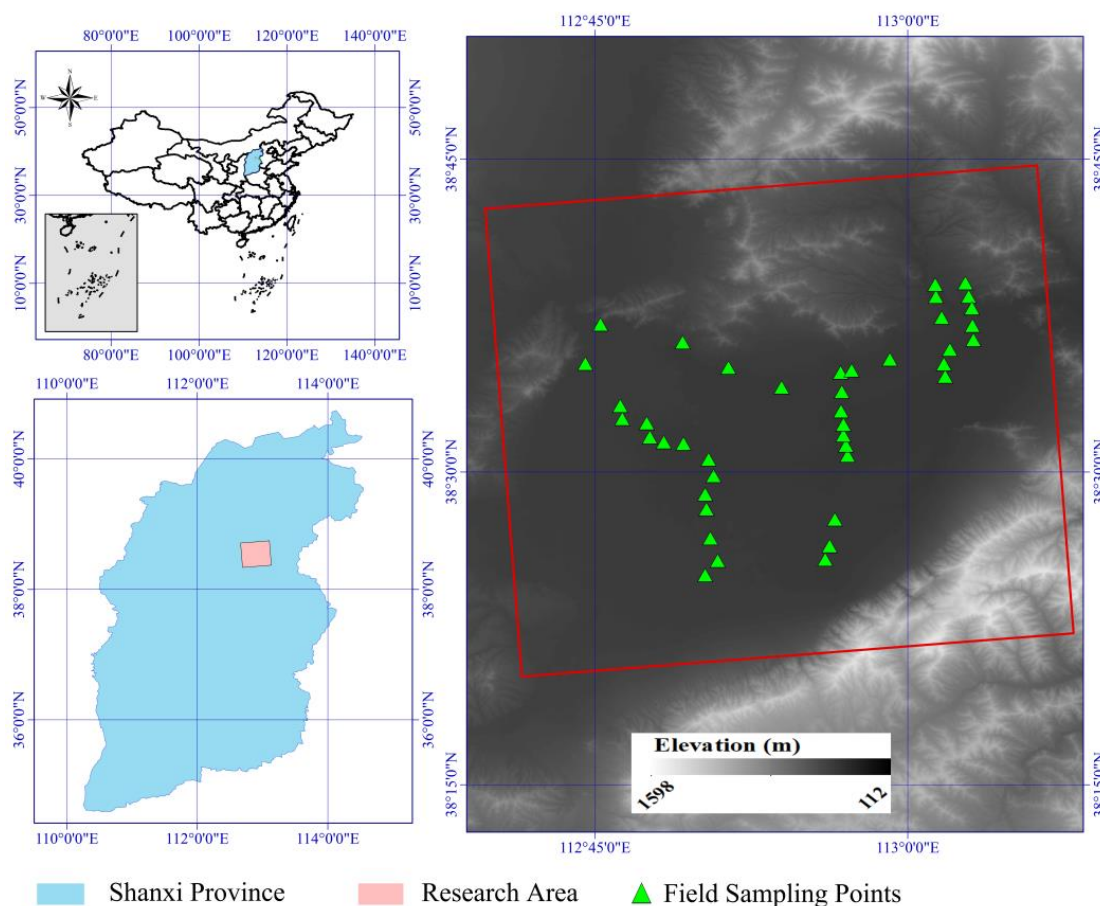


Figure 1. The study area and field-sampling points.

2.2. Field Samplings

The soil samples used in this research were collected at a depth of 10 cm from the soil surface and the GPS coordinates of each sampling point were recorded. Approximately 20 g of soil samples were collected by using cutting rings, and soil samples were placed in an aluminum box (85 cm³) to measure the soil moisture and its reflectance.

The soil-water content (SMC) mentioned in this paper refers to soil-moisture content per mass (SMC_g). The SMC_g is obtained with the thermogravimetric (oven-drying and weighing) method. The specific calculation process is:

$$SMC_g(g/g) = \frac{m_1 - m_2}{m_1 - m_0} \quad (1)$$

In Formula (1), m_0 is the mass of the dried, empty aluminum box, m_1 is the mass of the aluminum box and soil sample before drying and m_2 is the mass of the dried aluminum box and dried soil sample.

2.3. Soil-Reflectance Measurements

In this study, the soil reflectance was measured in the laboratory by using the SVC-1024i portable spectroscope. The soil samples were irradiated at an angle of 45° from the

halogen lamp, whose power was 50 watts (Lowel Light Pro., JCV 14.5 V-50 WC). Each sample was measured five times to reduce the measuring error and noise of the instrument.

2.4. Remote-Sensing Data and Preprocessing

In this study, GF-2, GF-3 and GF-5 remote-sensing data were used to estimate the soil moisture. The details of these three different remote-sensing data are shown in Table 1.

Table 1. Details of the GF-2, GF-3 and GF-5.

Satellites	GF-2	GF-3	GF-5
Resolution	1 m, panchromatic; 4 m, multispectral	1–500 m	20–40 m
Coverage	45 km	30–650 km	60 km
Revisiting period	5 d	<3 d	4 d
Wavelength	panchromatic, 450–900 nm multispectral, 450–890 nm	C band 1530–1565 nm	450–12500 nm
Date of image acquired	16 May 2019	24 May 2019	9 May 2019

The GF-2 is a high-resolution earth-observation satellite in a synchronous orbit. It was independently developed and made in China and has characteristics of high resolution (better than 1 m), multiple perspectives (panchromatic camera and multispectral camera) and short revisit time (merely 5 days). GF-2 data were pre-processed by radiometric calibration and atmospheric correction. The software ENVI was used to achieve radiometric calibration, and the atmospheric correction was completed by the FLAASH module.

The GF-3 is China's first C-band multiple-polarization synthetic-aperture radar (SAR) satellite. It was launched in August 2016 and can obtain stable and reliable high-resolution microwave-remote-sensing images [49]. The GF-3 can provide three modes and twelve types of microwave-remote-sensing data with a high accuracy (1–500 m) and a large coverage (30–650 km). The spatial resolution of the GF-3 varies from 1 m to 500 m with swaths from 10 km to 650 km. The SAR supports single polarization of HH or VV, dual polarization of HH+HV or VH+VV and quadruple polarization of HH + HV + VH + VV [50]. The GF-3 data used in this study were quadruple-polarization data (HH + HV + VH + VV) with a spatial resolution of 10 m. The GF-3 data were pre-processed by radiometric calibration, multi-look processing and filter processing. The PIE-SAR software was used to perform these operations to obtain the radar-backscattering coefficient.

The GF-5 is a satellite sensor of visible-shortwave infrared advanced hyperspectral imager (AHSI). It has the characteristics of a large width (60 km), a wide spectrum (450–2500 nm) and a high radiation resolution. The AHSI imager of the GF-5 satellite has 330 spectral bands from 450 nm to 2500 nm. The spatial resolution of GF-5 is 30 m. The pre-processing of the GF-5 images includes radiometric calibration and atmospheric correction. The ENVI software was used to perform radiometric calibration and atmospheric correction was completed by the FLAASH module.

3. Methods

3.1. Variables Selection

The purpose of the soil-moisture modeling was to construct the relationships between the variables extracted from remote-sensing data and the SMC_g . The first important step was selecting the variables for SMC_g estimation. The first candidate variable was the reflectance of the soil moisture. The second candidate variable was the continuum removed reflectance (CR reflectance) of the soil moisture, which can be calculated by using spectral tools of the commercial software ENVI 5.3.1 software (Exelis VIS, Silicon Valley, CO, USA). To increase the number of candidates in the independent-variable dataset, the

spectral indices, vegetation indices and other parameters of the images of three different spatial resolutions from GF-2, GF-3 and GF-5 were extracted as candidate characteristic variables. Furthermore, the Pearson correlation coefficient between candidate remote-sensing variables and the SMC_g field measurements was calculated, and the variables with lower correlation coefficients ($R < 0.05$) were removed to improve the quality of the candidate remote-sensing variables.

The vegetation index (VI) was calculated by the formula below [51]:

$$VI = \frac{Band_i - Band_j}{Band_i + Band_j} \quad (2)$$

VI is the vegetation index. $Band_i$ and $Band_j$ are the measured spectral reflectance on bands i and j , respectively.

3.2. Modeling of the Soil-Moisture Estimation Based on Multi-Source Remote-Sensing Data

In this study, we used the linear method and the non-linear method to establish the soil-moisture estimation model and compared the differences between the results. The flow chart is shown in Figure 2.

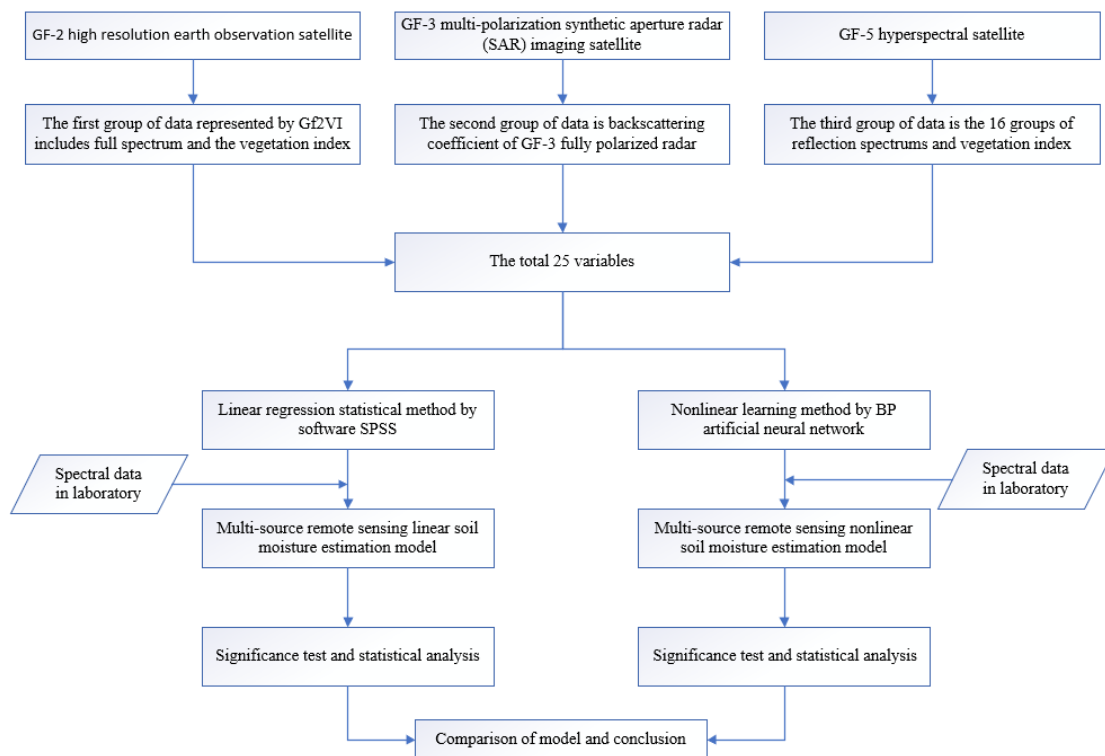


Figure 2. Flow chart of the soil-moisture estimation by using multi-source remote sensing.

3.2.1. Linear Method

The linear model of the soil moisture was established by using the method of least squares. First, the relationship between remote-sensing parameters extracted from three different remote-sensing data was calculated. The remote-sensing parameters included the reflectance of each band of different sensors, continuum-removal reflectance and the vegetation indices, which were calculated by the method in Section 3.1. Next, the linear model of soil-moisture estimation was established by using the least-squares method. The SPSS software helped us to achieve this purpose (SPSS 20.0, Inc., Chicago, IL, USA; Microsoft Corp., Redmond, WA, USA).

3.2.2. Erf-BP Artificial-Neural-Network Model

Non-linear learning is a method of modeling in which the relationship between the independent variable and the dependent variable cannot be described by a one-variate or multi-variate linear function. As advanced learning algorithms, artificial neural networks (ANN) are capable of approximating or learning complex mapping relationships with multi-dimensional variables [52]. Remote-sensing images have large dimensions and are nonlinear; therefore, the use of artificial neural networks (ANN) became one of the most common methods in the field of quantitative remote sensing [53,54]. Back-propagation neural networks are one of the most commonly used ANN algorithms. The conventional back-propagation (BP) algorithm has some problems, such as its slow rate of convergence, local optimization of overfitting and result-improvement difficulties [55,56]. Therefore, a modified BP neural network was developed by using the Gaussian function.

The Gaussian function is a non-elementary function. It has a wide range of applications in probability theory, statistics and partial differential equations. The definition of the Gaussian function [57] is:

$$\text{erf}(x) = \frac{2}{\sqrt{\pi}} \int_0^x e^{-t^2} dt \tag{3}$$

The Erf-BP neural network is a new algorithm that uses the Gaussian function as a new activation function of the hidden layer. Furthermore, the logsig function is used as the activation function of the output layer.

The algorithm of the output node can be found as follows: Formula (4) is the algorithm of the output of the hidden node, and Formula (5) is the algorithm of the output of the output node:

$$y^{(k)} = \text{erf}\left(-\frac{X^{(k)} \cdot IW}{\sqrt{\lambda}}\right) \tag{4}$$

$$O^{(k)} = \frac{1}{(1 + \exp(-y^{(k)} \cdot LW))} \tag{5}$$

In the Formula (4), $X^{(k)}$ represents the k -th sample, $k = 1, 2, \dots, n$. $y^{(k)}$ is the output of the hidden node, $O^{(k)}$ is the output of the output node, IW is the connection-weight value from the output layer and the hidden layer (including the threshold) and LW is the connection-weight value from the hidden layer and the output layer (including the threshold).

The error-correction algorithm from the hidden node to the output node of the output layer is as follows:

$$\delta^{(k)} = (t^{(k)} - O^{(k)}) \cdot O^{(k)} \cdot (1 - O^{(k)}) \tag{6}$$

In Formula (6), $\delta^{(k)}$ is the error correction of the k -th sample in the output layer and $t^{(k)}$ is the expected value of the k -th sample in the output node.

The error-correction algorithm from the output node to the hidden node of the hidden layer is as follows:

$$\varphi_{.h}^{(k)} = \delta^{(k)} \cdot LW'_{h.} \cdot \frac{2}{\sqrt{\pi}} \exp\left(-\frac{\gamma_{.h}^2}{\lambda}\right) \tag{7}$$

In Formula (7), γ is the h -th column value of the k -th sample error correction in the hidden layer, $LW'_{h.}$ is the k -th row transpose and $\gamma_{.h}$ is the h -th column value of the weighed product between k -th sample and IW .

The sample-data set was divided in proportion to three independent data subsets, which included a training sample, a validation sample and an independent sample. The weights of the three parts are determined by the principle of a minimum of the root-mean-square error. The goal of the learning process is to make the output values as close

as possible to the actual values by using cyclic correction. For a training sample s , the calculation of the mean-square error E_s is as follows:

$$E_s = \frac{1}{2} \sum_1^k (t_k - o_k)^2 \quad (8)$$

In Formula (8), t_k is the k -th expected output value and o_k is the corresponding actual output value.

The total root-mean-square error is represented as:

$$E = \frac{1}{n} \sum E_n \quad (9)$$

In Formula (9), n is the total of the samples.

The weight of the samples can be calculated by the following formula:

$$w(k+1) = w(k) + \eta(k)D(k) + a(w(k) - w(k-1)) \quad (10)$$

In Formula (10), $w(k+1)$, $w(k)$ and $w(k-1)$ are the new weight, current weight and previous weight, respectively. η is the learning rate. Index a is used to avoid overfitting.

The estimation efficiency of the net can also be calculated by the self-adaption adjustment of the learning rate, as in Formula (11):

$$\eta(k) = 4^\epsilon \eta(k-1) \quad (11)$$

where ϵ is the adjustment coefficient, which can be calculated as follows:

$$\epsilon = \text{sign}(D(k)D(k-1)) \quad (12)$$

In Formula (12), $D(k)$ is the negative gradient of the moment samples; it is defined as follows:

$$D(k) = \left(\frac{E(w)}{w} \right) \quad (13)$$

In Formula (13), w is the current weight $w(k)$ in Formula (10).

In this study, we developed a new three-layer BP artificial neural network, as shown in Figure 3. It includes an input layer, a hidden layer and an output layer. The input layer is the data set of independent variables, which is determined by the correlation coefficient between remote-sensing variables and soil moisture. The hidden layer is a modified BP neural network. The main characteristics of this Erf-BP artificial neural network are its reduced memory unit and excellent learning and memory ability [57,58]. Furthermore, the number of hidden layers was a variable. The results of different hidden layers of BP are compared in the Results section. The output layer is the soil-moisture content per mass (SMC_g). In order to solve the problem of the limitation of the sampling number, we chose the cross-validation approach to evaluate the efficiency of the neural network. In addition, we created a 10-fold cross-validation program by using the MATLAB R2017a software (MathWorks Inc., Natick, MA, USA) to compute the estimating error of the artificial neural network.

3.3. Validation

In this study, the correlation coefficient (R), coefficient of determination (R^2), root-mean-square errors (RMSE) and mean absolute error (MAE) were selected to evaluate the precision. Specific formulas are shown below [59]:

$$R = \frac{\text{Cov}(x_i, y_i)}{\sqrt{\text{Var}[x_i]\text{Var}[y_i]}} \quad (14)$$

$$R^2 = 1 - \frac{\sum_{i=1}^n (y'_i - y_i)^2}{\sum_{i=1}^n (y'_i - \bar{y})^2} \quad (15)$$

$$RMSE = \sqrt{\frac{1}{n} \sum_{i=1}^n (y'_i - \bar{y})^2} \quad (16)$$

$$MAE = \frac{1}{n} \sum_{i=1}^n |y'_i - y_i| \quad (17)$$

In Formulas (14)–(17), x_i is the spectral data or remote-sensing variables and y_i , y'_i and \bar{y} are the SMC_g measurement, estimation and average value, respectively.

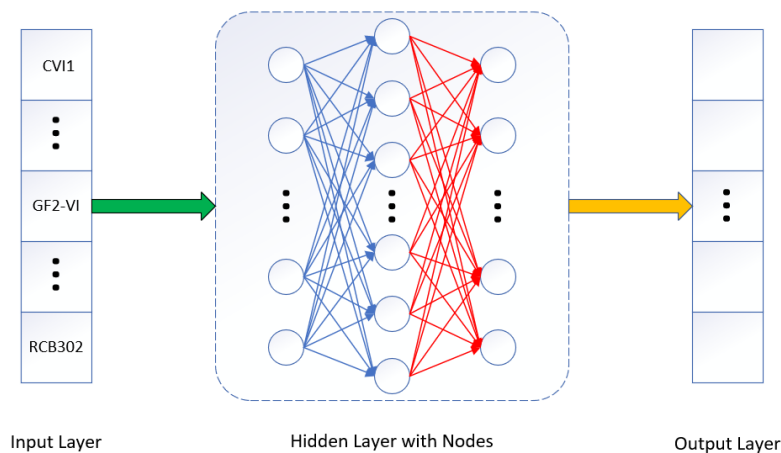


Figure 3. Schematic diagram of the BP artificial neural network used in this study.

4. Results

4.1. Spectral Response of Soil Moisture to Reflectance

To compare the effect of soil moisture on its reflectance, different soil samples with various degrees of soil moisture were selected and their reflectances were compared. Various levels of soil moisture were plotted, with SMC_g from 0.090 g/g to 0.203 g/g; their reflectances on the VIS-NIR band from 400 nm to 2500 nm are shown in Figure 4. The results showed that the reflectance of the soil samples decreased when their SMC_g increased. The two absorption peaks, approximately 1470 nm and 1940 nm, are presented in Figure 4. Furthermore, the depth of the absorption of the reflectance in these two bands increased with the increasing soil moisture [13]. This phenomenon was caused by the fundamental absorption by OH^- groups of water molecules in soil [60]. These results were consistent with those of other studies [61–63].

4.2. Analysis of the Correlation between Soil Moisture and Its Reflectance

4.2.1. Analysis of the Correlation between Soil Moisture and Its Reflectance

The statistical correlation coefficient is one of the most commonly used indicators for the variables selection. A large correlation coefficient means a significant linear relationship. The correlation coefficient between the soil reflectance and its SMC_g was calculated by using the SPSS software. The results are shown in Figure 5. There was a positive correlation between the SMC_g and its reflectance in the visible light band. The correlation coefficient decreased at the visible light band with a wavelength before 900 nm. The highest positive-correlation coefficient was 0.2545 at 400 nm. Furthermore, there was a negative correlation between the SMC_g and its reflectance in the near-infrared (NIR) and shortwave infrared (SWIR) wavelengths. The absolute value of the correlation coefficient between the SMC_g and its reflectance increased with the increase in the wavelength of the reflectance. The minimum negative-correlation coefficient was -0.5129 at 1940 nm. Furthermore, two absorption peaks, approximately 1470 nm and 1940 nm, can also be found in this analysis.

These results are similar to those of many other studies [64]. The reflectance at the wavelengths which had the maximum and minimum coefficients of correlation with the soil moisture was selected as the candidate variables.

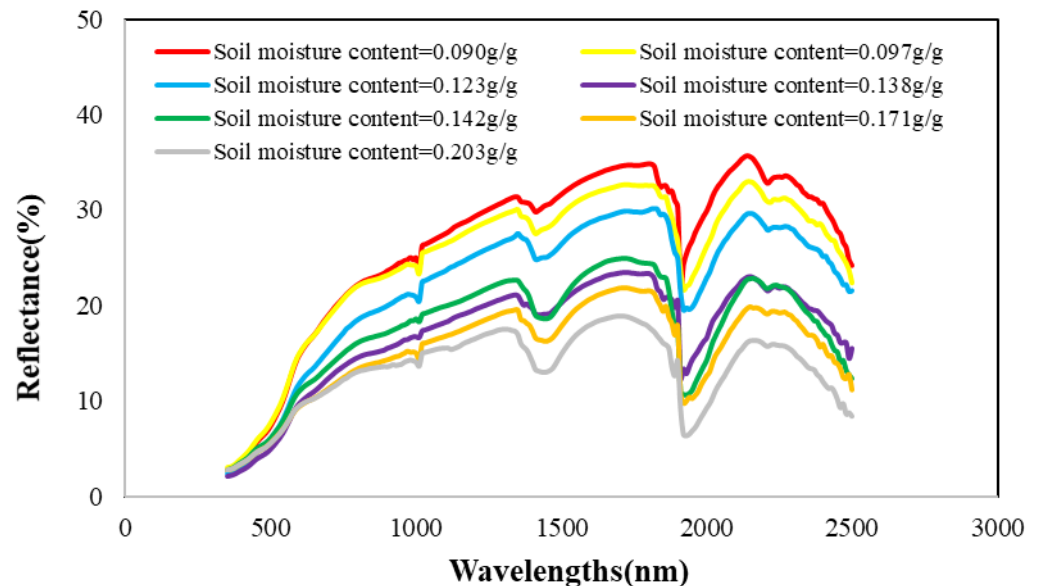


Figure 4. The soil reflectance with various soil-moisture contents.

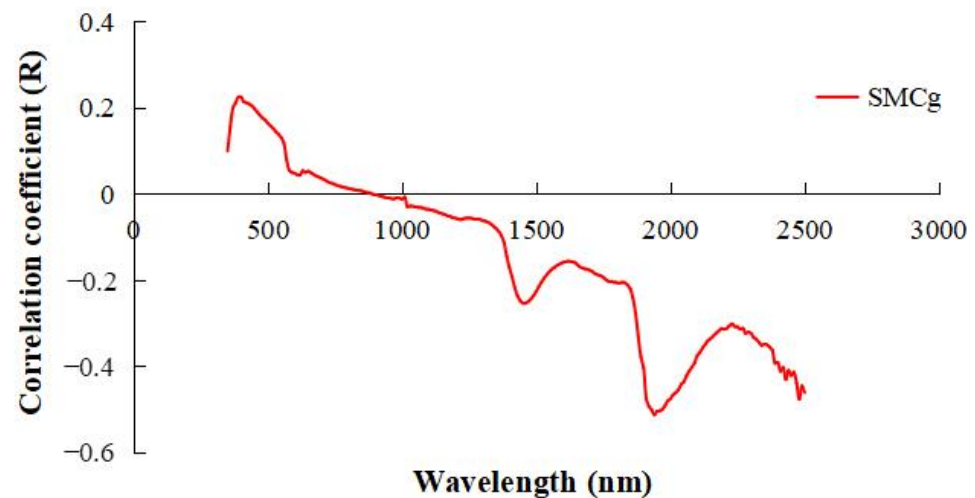


Figure 5. Correlation coefficients between SMC_g and its reflectance.

The correlation coefficients between the continuum-removal reflectance and the SMC_g are shown in Figure 6. The results showed that there was a positive correlation from 350 nm to 1100 nm and a negative correlation from 1100 nm to 2500 nm, except for 1290 nm, 1650 nm, 1830 nm and 2230 nm because there were two small positive-correlation relationships at these bands. Figure 6 also indicates that four parts of the highly related bands were correlated with the SMC_g which are located at the wavelengths approximately 440 nm, 1470 nm, 2050 nm and 2230 nm on the continuum-removal reflectance curves. The highest positive-correlation coefficient was 0.5014 at 2230 nm and the highest negative-correlation coefficients was -0.8599 at 2050 nm. Furthermore, the continuum-removal reflectance at the wavelength which had the maximum and minimum coefficients of correlation with the soil moisture, was selected as a candidate variable.

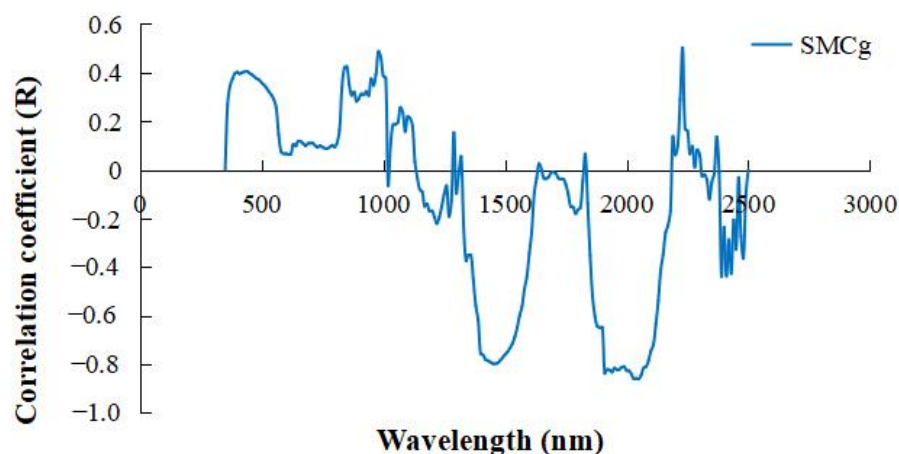


Figure 6. Correlation coefficients between the SMC_g and its continuum-removal reflectance.

Compared with the results of the original reflectance, the correlation coefficient between the continuum-removal reflectance and soil-moisture content (SMC_g) was larger than that of the original reflectance; the results indicated that there was a more significant linear relationship between the continuum-removal reflectance and the SMC_g . At the same time, the spectral-absorption characteristics caused by the soil moisture were more obvious than those of the original reflectance.

4.2.2. Analysis of the Correlation between Soil Moisture and VIs

To identify more and better independent variables, we attempted to build a vegetation index (VI) by combining any two bands. We calculated all of the VIs of the combination of any two bands, followed by the equation of $(B1 - B2)/(B1 + B2)$, after which we calculated the correlation coefficients between the VIs and the soil moisture. The correlation-coefficient results are shown in Figure 7. The value of each point in this figure is the correlation coefficient between the SMC_g and the VI, which is calculated from the reflectance at corresponding wavelengths on the x and y axes following the equation of $(B1 - B2)/(B1 + B2)$. The results showed that the highest correlation coefficient between the soil-moisture content and the VI was 0.3143, which was calculated by using the reflectance of the wavelength at the combination of the 390 nm and 400 nm bands. The minimum value of the correlation coefficient was -0.4885 , which was calculated by using the wavelength at the band combination of 1930 nm and 1940 nm. Therefore, these two significant and related VIs were selected as the candidate variables. The results also indicated that the correlation relationship between the soil-moisture content and its VI improved.

At the same time, we resampled the reflectance of the laboratory measurement by using the filter function of the GF-2 and GF-5, after which the VIs based on the GF-2 and GF-5 remote-sensing data were calculated and the correlation-coefficient results were obtained. The best VI of the GF-2 remote-sensing data was the blue-and-green-band combination with an R of 0.4701. For the GF-5 data, the highest correlation coefficient between the soil-moisture content and the VI based on the GF-5 satellite data was 0.552, which was calculated by using the wavelength at the band combination of 1240.76 nm and 1266.1 nm. The lowest correlation coefficient was at the wavelength of the band combination of 1948.57 nm and 2167.73 nm with an R of -0.544 . These two VIs were also selected as the candidate variables.

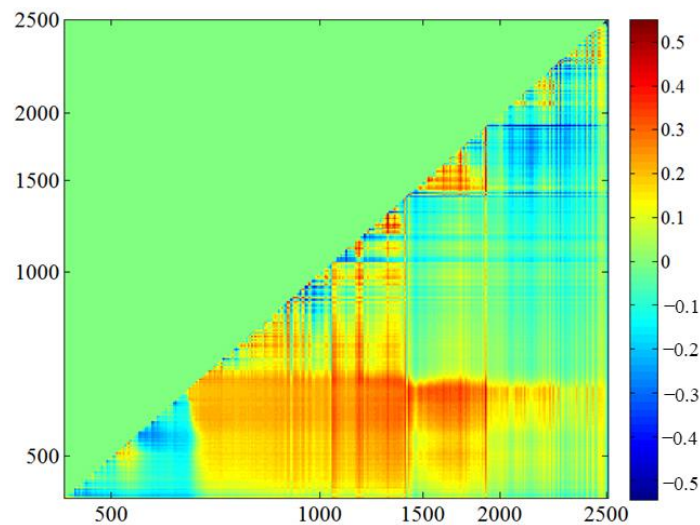


Figure 7. Correlation coefficient between SMC_g and VIs.

4.2.3. Correlation Analysis between the Polarization Parameters and SMC_g

The backscattering coefficients of the four polarization modes were extracted from the GF-3 microwave-polarization data. Next, the correlation coefficients between the parameters extracted from the microwave-polarization modes and the SMC_g were calculated. The parameters extracted from the microwave polarization included the backscattering coefficients of HH (σ_{HH}), VV (σ_{VV}) and the mean of the backscattering coefficients (σ_{VH}) of VH and HV. The results are shown in Figure 8. The correlation coefficients between the various microwave-polarization modes and the soil-moisture content ranged from -0.0522 to 0.1643 ; the best was σ_{VH} , with an R of 0.1643 .

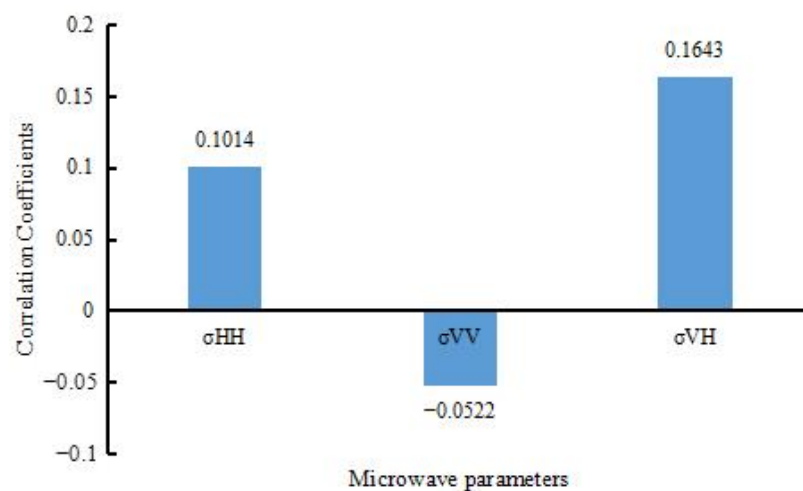


Figure 8. The correlation coefficients between microwave-polarization modes and SMC_g .

4.3. Soil-Moisture-Estimation Modeling Using Linear Method

4.3.1. Soil-Moisture-Estimation Model Based on GF-2

According to the statistical analysis results, the highest significant linear-related parameter of single-resource remote-sensing data was screened out, and the SMC -estimation model of the single-resource remote-sensing data was established. For the GF-2 data, the VI combining the blue band and green band from the GF-2-high-resolution data was the highest related to the SMC_g , and the linear-regression model was established as follows:

$$SMC_g = 0.452 \times VI_{G-B} + 0.243$$

The coefficient of determination of the model based on the GF-2 high-resolution remote-sensing data was 0.221 and the RMSE was 0.032 g/g. The model and its coefficient passed the significance test.

4.3.2. Soil-Moisture-Estimation Model Based on GF-3

Referring to the step above, the linear-regression model based on the parameters of the polarization modes from the GF-3-microwave-remote-sensing data was established as follows:

$$SMC_g = 0.0694 \times \sigma_{VH} + 0.1511$$

The coefficient of determination of the model based on the GF-3-microwave-remote-sensing data was 0.027 and the RMSE was 0.023 g/g. The model and its coefficient passed the significance test.

4.3.3. Soil-Moisture-Estimation Model Based on GF-5

In a similar way, the linear-regression model of SMC_g estimation based on the GF-5 hyperspectral data was established as follows:

$$SMC_g = 1.263 \times VI_{CVI} + 0.144$$

In this model, the SMC_g is the soil moisture per mass, and the VI_{CVI} is the vegetation index calculated based on the bands B179 (1240.76 nm) and B182 (1266.1 nm) of GF-5. The correlation coefficient of the model based on the GF-5 hyperspectral remote-sensing data was 0.53 and its RMSE was 0.020 g/g. The model and its coefficient passed the significance test.

4.4. Multiple-Linear-Regression Model Based on Multiple-Resource Remote Sensing

According to the results of the statistical analysis above, some parameters that were significantly and linearly related to the SMC_g were selected and a multiple-linear-regression model was established by using the SPSS software. Furthermore, the model of the SMC_g estimation based on multiple-resource remote sensing was established as follows:

$$SMC_g = 0.98 \times CVI1 + 0.471 \times VI_{G-B} + 0.097 \times RCB302 + 0.161$$

where y is the soil-mass moisture content (SMC_g). $CVI1$ is the vegetation index calculated by the continuum-removal spectrum on B179 (1240.76 nm) and B182 (1266.1 nm) from the GF-5 reflectance. VI_{G-B} is the vegetation index calculated by the blue and green bands of the GF-2. The $RCB302$ is the continuum-removal spectrum value on the GF-5 302 band (2277.29 nm). The correlation coefficient of the model is 0.732. The RMSE of the model is 0.017 g/g. The MAE is 0.517. The linear model and its coefficients passed the significance test.

Compared with the three different one-variable linear SMC_g estimation models using single-resource remote-sensing data, the multiple-linear-regression model using multiple-resource remote sensing had a higher correlation relationship and better accuracy. However, the linear-regression model based on the statistics method still could not perfectly optimize the model due to many factors, such as different sensors, different sensible bands, compatibility between the datasets, etc. Therefore, the nonlinear learning method could be used to ease and even solve the problem.

4.5. Soil-Moisture Estimation Based on Erf-BP Neural Network

The Erf-BP neural network is a modified neural network based on the method in Section 3.2.2. It is a three-layer neural network, including an input layer, an output layer and a hidden layer. The input layer includes three nodes, which were used to input the independent variables extracted from the multiple-resource remote-sensing data. The output layer included one node of soil-moisture estimation. The hidden layer was used

to fit the parameters of the neural network based on the Gaussian function. The model parameters' settings included the maximum training times and the training goal. The maximum training time was 5000, and the training goal was 0.01. The number of nodes in the hidden layer was determined by the method in Section 3.2.2. The final number of nodes in the hidden layer was between four and thirteen. We divided the samples into two groups of 75% and 25%; the group with 75% of the samples was used to train the neural network, and the group with 25% of the samples was used for the predictions. To increase the credibility of the results, we chose the cross-validation approach to evaluate the efficiency of the neural network. We tested the Erf-BP neural network with various nodes in the hidden layer and then determined the optimal Erf-BP neural network. The correlation coefficients of the RMSE between the soil moisture measured and predicted by different nodes of the hidden layer can be found in Table 2. The table showed that the accuracy of the soil-moisture estimation varied with the number of nodes in the hidden layer. When the number of hidden layers was nine, this neural network produced a best-fitting result with a training correlation coefficient and RMSE of 0.982 and 0.0272 g/g, respectively, a predicting coefficient and RMSE of 0.6650 and 0.0256 g/g, respectively, and an overall accuracy and RMSE of 0.6838 and 0.0146 g/g, respectively, and the MAE is 0.0082.

Table 2. Erf-BP neural network model using multiple remote-sensing data.

Number of Nodes of the Hidden Layer	Training Accuracy (R)	Training RMSE (g/g)	Prediction Accuracy (R)	Prediction RMSE (g/g)	Overall Accuracy (R)	Overall RMSE (g/g)
4	0.9455	0.0141	0.5553	0.0301	0.4790	0.0248
5	0.9627	0.0097	0.5654	0.0342	0.4787	0.0256
6	0.9767	0.0047	0.5956	0.0350	0.4983	0.0241
7	0.9789	0.00356	0.5854	0.0332	0.5284	0.0237
8	0.9801	0.00295	0.5583	0.0337	0.5781	0.0235
9	0.9827	0.00272	0.6650	0.0256	0.6838	0.0146
10	0.9741	0.00238	0.5753	0.0339	0.4775	0.0234
11	0.9782	0.00285	0.5354	0.0349	0.5787	0.0232
12	0.9730	0.00367	0.5116	0.0350	0.5151	0.0355
13	0.9805	0.00442	0.5163	0.0301	0.4515	0.0292

As shown in Figure 9, the fittings and training precisions varied with the number of nodes in the hidden layer. The correlation coefficients of the training-network fittings ranged from 0.9455 to 0.9827. The prediction correlation coefficients of the test-network fittings ranged from 0.5116 to 0.6650. The correlation coefficients of the synthesis-evaluation network ranged from 0.4515 to 0.6838. The standard errors of the different BP neural-network-estimation results were also different, and the overall RMSE ranged from 0.0146 to 0.0355 g/g. After the synthesis evaluation, the BP neural network with nine nodes in the hidden layer had the best performance and the highest prediction precision. The correlation coefficient of the training network was 0.9827, and the prediction accuracy was 0.6650. The overall RMSE of the model was 0.0146 g/g.

The scattering plot of the SMC_g measured and estimated by using the Erf-BP artificial neural network is shown in Figure 10. The results showed that there was a near-perfect goodness of fit between the predicted and measured soil-moisture contents. The scatter points were positioned closely around the directly proportional function $y = x$. This showed that the Erf-BP artificial neural network can correctly describe the nonlinear relation between the independent variables and soil-moisture content. Therefore, it also has a satisfying prediction accuracy ($RMSE = 0.0146$ g/g). Based on this analysis, we chose the Erf-BP artificial neural network model with nine nodes in the hidden layer as the soil-moisture estimation model.

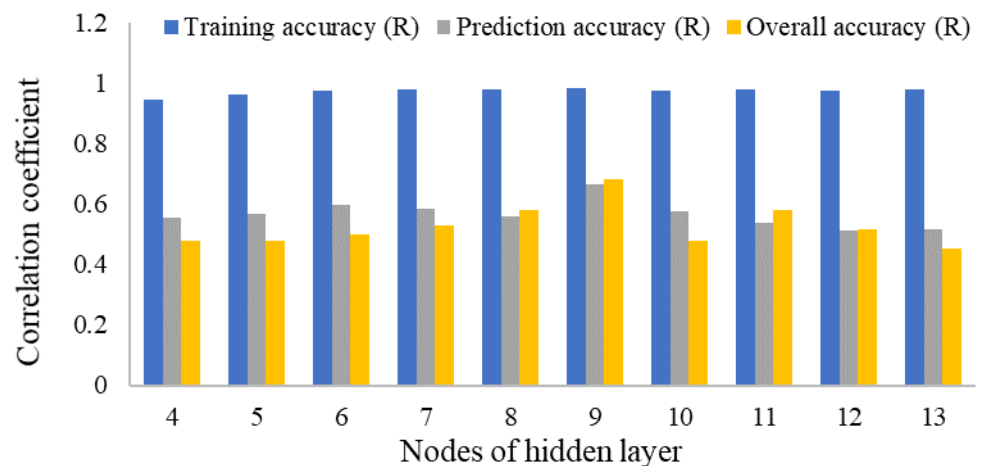


Figure 9. Comparison of Erf-BP neural-network modeling with various of hidden-layer nodes.

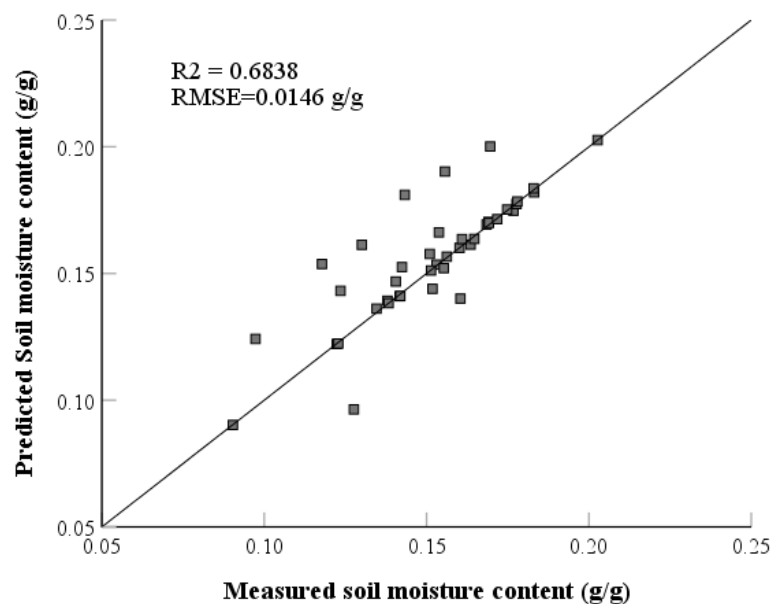


Figure 10. Scattering plot between SMC_g measured and estimated by using Erf-BP artificial neural network with 9 hidden layer nodes.

5. Discussion

Soil moisture plays a key role in the hydrological cycle involving land, atmosphere and water bodies [1]. As the material basis for plant growth, soil moisture affects the distribution of vegetation on the land surface [65]. Photosynthesis, respiration, transpiration and other life activities of plants are also dependent on soil moisture, which has a major impact on crop growth and agricultural production [66]. At the same time, variations in the soil moisture affect the water transfer between land, the atmosphere and even water bodies, as well as significantly affect the carbon cycle of land-based ecological systems [67,68]. Therefore, it is very significant to estimate and predict the spatial and temporal distribution of soil moisture with high accuracy.

5.1. Analysis of Single-and Multiple-Resource Remote-Sensing Data

The soil-moisture-acquisition method includes field measurements and estimations involving the use of remote sensing and hydrological-model simulations. Owing to the advantages of remote sensing, such as its wide coverage, low cost, multi-temporal and multi-resolution properties, and characterization of spatial distribution and monitoring of surface changes, it has become an important tool in the monitoring of soil-moisture infor-

mation on the local or global scale [48,69]. Furthermore, various methods of soil-moisture estimation are reported, and their advantages and disadvantages are discussed [69,70]. Compared with single-resource remote-sensing data, many studies show that it is more efficient to estimate SMC by integrating high-resolution, hyper-spectral and microwave-remote-sensing data [71–73]. In this paper, we used high-resolution, microwave and hyper-spectral data to establish the SMC-estimation models, respectively. However, the models established by using the single-resource remote-sensing data have their respective problems, which cause them to display unreliable accuracy [21]. For example, SMC-estimation models based on high-resolution (GF-2) data and hyperspectral (GF-5) data both belong to optical-remote-sensing SMC-estimation models. Optical methods are generally based on the relationship between the soil moisture content and its spectral reflectance. The combination of high-resolution and hyperspectral remote-sensing images increases the spectral information of the surface to ensure the accuracy of SMC estimation and improve its spatial resolution with the help of high-resolution remote-sensing data. However, the disadvantage of the optical methods is that vegetation cover on the soil surface can reduce the soil-radiation information and thus affect the accuracy of soil-moisture estimation [74]. At the same time, the optical-remote-sensing model shows its weakness when it encounters bad weather such as clouds, fog and water vapor [75]. Consequently, the disadvantages of the optical-remote-sensing method can be overcome in areas with bare soil and sparse vegetation. Fortunately, the soil samples were collected in spring for this paper; therefore, it was not necessary to consider this factor in this study [76,77].

In comparison, the microwave-remote-sensing technique presented high sensitivity to soil moisture, and it has become an effective method for soil-moisture estimation [78,79]. In this study, the SMC-estimation model was established based on microwave (GF-3) data [80]. It offers some advantages, such as strong penetration and the lack of influence from clouds [81]. However, it also has its limitations, such as the influence of large-coverage or extreme weather in the atmosphere and image-information-loss caused by noise [82]. The combined optical-and -microwave-remote-sensing method can not only ensure the high soil-moisture sensitivity of microwave data but also increase the richness of surface information from optical-remote-sensing data. Meanwhile, the influence of vegetation on microwave-soil-moisture estimation was inevitable. To correct this uncertainty caused by vegetation, optical-remote-sensing can also be used to extract vegetation parameters and help to eliminate the effect of vegetation on microwave-remote-sensing data [69,83]. In addition, with constraints on antenna size and the altitude of low Earth orbits, some of the microwave-remote-sensing presented data with a low spatial resolution. By contrast, the optical-remote-sensing data also had a high spatial resolution; the combination of the optical and microwave data can generate soil-moisture estimations with sufficient accuracy and a higher spatial resolution [84].

Compared with these single-resource SMC-estimation models, the linear and nonlinear models based on multiple-resource remote-sensing data have higher accuracies and better correlations. In particular, the nonlinear model based on the Erf-BP neural network has the highest accuracy, with an overall RMSE of 0.0146 g/g, and the best overall-correlation coefficient, with an R of 0.6838. The results of this study show that by integrating different types of remote-sensing data, the model can offer SMC-estimation with superior accuracy and solve the problems of single-resource remote sensing in SMC-estimation described above [85,86].

5.2. Analysis of the New Erf-BP Artificial-Neural-Network Method

For multiple-resource remote-sensing data modeling, the normal multiple-linear-regression-model method and the conventional machine-learning method have some limitations [87,88]. For example, the normal multiple-linear-regression method fails to weigh the complexity of various factors in multiple-resource remote-sensing data [89]. This is because this statistical method assumes that this relationship is linear in one or more dimensions. However, many remote-sensing processes are not linear, but non-linear [53].

Compared with the linear model, the non-linear-modeling method may obtain better-fitting results. The conventional artificial neural network method improves the ability to weigh the complexity of various factors. However, the traditional BP neural network features some disadvantages, such as its slow training speed and low accuracy [90]. The conventional artificial-network method also has its problems, including a disordered weight-adjustment definition, the ambiguity of hidden layer nodes, the local optimization of overfitting and a slow convergence rate [91]. To overcome these disadvantages, a new Erf-BP artificial neural network used the Gaussian function to increase the convergence rate. A novel algorithm was then introduced to optimize the number of hidden-layer nodes and determine the training network, the verification network and the prediction network. The overall correlation coefficient of the SMC-estimation results based on the Erf-BP artificial neural network was enhanced from 0.4515 to 0.6838. The accuracy of the SMC model was increased, and the RMSE decreased from 0.0260 g/g to 0.0146 g/g. By comparison, the correlation coefficient and accuracy of SMC-estimation were better than those of the multiple-linear-regression model [92].

5.3. Uncertainty

The first uncertainty of this algorithm is the time synchronization problem. The multiple-resource remote-sensing data are not strictly time synchronized due to the different orbit parameters and satellite orbit period. We corrected this asynchronization error by using a simple linear model based on the field measured reflectance. The relationship between the measured and remote-sensing reflectance data obtained is shown in Figure 11. The figure shows that there will be uncertainty error for the estimation of soil moisture because of the time asynchronization of remote-sensing data with field measurements. The reflectance extracted from remote-sensing data were deviated from the measured results in Figure 11. Moreover, a linear relationship between the remote-sensing data and the field-measured reflectance will help us to correct this error as much as possible. However, there were no field backscattering property measurements, so the uncertainty error of time asynchronization of SAR still existed. This uncertainty error of time asynchronization will have effect on the soil moisture results estimated from the remote-sensing data. This problem should be discussed in the future.

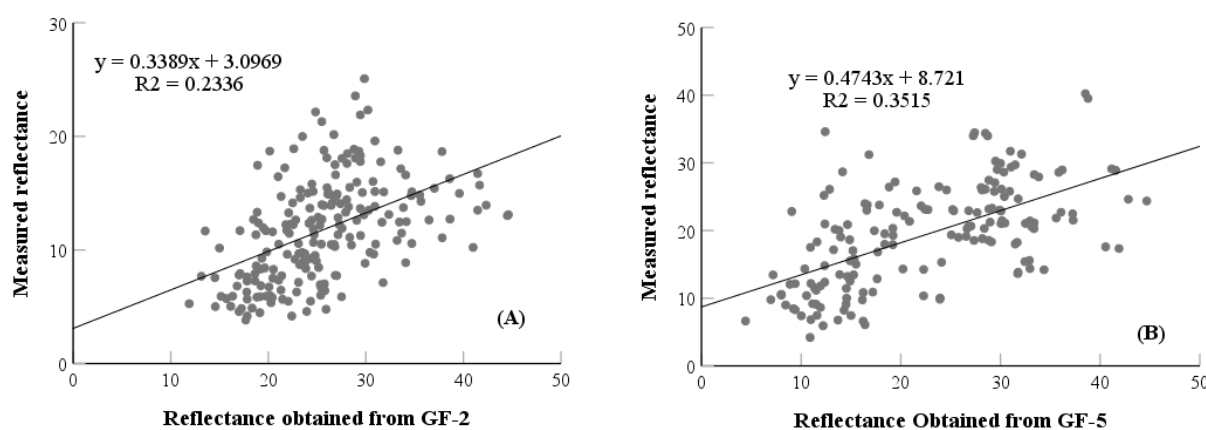


Figure 11. Scattering plot between reflectance measured and obtained from remote-sensing data of GF-2 and GF-5. (A) Scattering plot of GF-2; (B) scattering plot of GF-5.

Almost all algorithms have limitations. In this study, we did not consider the effect of surface roughness on microwave-remote-sensing data. Furthermore, vegetation cover was also not considered in the study since the field sampling took place in the spring and the plants had not yet begun to grow. Therefore, we assumed that the plants above the soil surface were bare, and their impact on the results was ignored.

We expect to establish a more comprehensive soil-moisture estimation and prediction system by considering the influencing factors, including topographic factors, soil properties

and so on [93,94]. Furthermore, we will attempt to improve the algorithm by using the Bayesian framework, updating the genetic algorithm, and applying other new methods that can help us perform SMC-estimations over a large region with high accuracy [47,95].

6. Conclusions

In this work, a soil-moisture-estimation model using multiple-resource remote-sensing data was established, and the comparison of the modeling results between single- and multiple-resource remote-sensing data were shown. Some significant and useful conclusions were obtained, as follows:

- (1) Compared with the single-resource remote-sensing SMC-estimation model, the soil-moisture-estimation model using multiple-resource remote-sensing data offered better accuracy with a correlation coefficient of 0.732. The RMSE of the model was 0.017 g/g. However, the correlation coefficient only ranged from 0.401 to 0.53 and the RMSEs were between 0.02 g/g and 0.0466 g/g for the single-resource remote-sensing data estimation results. Furthermore, the correlation and accuracy of the SMC-estimation model using multiple-resource remote-sensing data can be efficiently improved.
- (2) The non-linear neural network model can further improve the prediction accuracy of the SMC-estimation. The overall correlation coefficient of the SMC-estimation results based on the Erf-BP artificial neural network was enhanced from 0.4515 to 0.6838. Compared with the results of the multiple linear models, the accuracy of the SMC-estimation was increased, and the RMSE decreased from 0.017 g/g to 0.0146 g/g.

Author Contributions: X.Y. conceived and designed the experiments; T.M. performed the experiments and analyzed the data; T.M. and X.Y. wrote the paper; X.Y., Y.Y. and G.L. reviewed and edited the paper. All authors have read and agreed to the published version of the manuscript.

Funding: This research was funded by the National Natural Science Foundation of China, grant number 31971580, 31870621; the Fundamental Research Funds for the Central Universities of China, grant numbers 2572019BA10, 2572021BA08 and 2572019CP12; the China Postdoctoral Science Foundation, grant number 2019M661239; and the Innovation and Entrepreneurship Training Program for College Students, grant number 202110225089.

Conflicts of Interest: The authors declare no conflict of interest.

References

1. Babaeian, E.; Sadeghi, M.; Jones, S.B.; Montzka, C.; Vereecken, H.; Tuller, M. Ground, Proximal, and Satellite Remote Sensing of Soil Moisture. *Rev. Geophys.* **2019**, *57*, 530–616. [[CrossRef](#)]
2. Kumar, S.V.; Dirmeyer, P.A.; Peters-Lidard, C.D.; Bindlish, R.; Bolten, J. Information theoretic evaluation of satellite soil moisture retrievals. *Remote Sens. Environ.* **2018**, *204*, 392–400. [[CrossRef](#)]
3. Sela, S.; Svoray, T.; Assouline, S. Soil Surface Sealing Effect on Soil Moisture at a Semiarid Hillslope: Implications for Remote Sensing Estimation. *Remote Sens.* **2014**, *6*, 7469–7490. [[CrossRef](#)]
4. Evans, S.; Allison, S.; Hawkes, C. Microbes, memory and moisture: Predicting microbial moisture responses and their impact on carbon cycling. *Funct. Ecol.* **2022**, *36*, 1430–1441. [[CrossRef](#)]
5. Wagner, W.; Scipal, K.; Pathe, C.; Gerten, D.; Lucht, W.; Rudolf, B. Evaluation of the agreement between the first global remotely sensed soil moisture data with model and precipitation data. *J. Geophys. Res.-Atmos.* **2003**, *108*, 4611. [[CrossRef](#)]
6. Zhang, X.C.; Yuan, X.; Liu, H.R.; Gao, H.S.; Wang, X.G. Soil Moisture Estimation for Winter-Wheat Waterlogging Monitoring by Assimilating Remote Sensing Inversion Data into the Distributed Hydrology Soil Vegetation Model. *Remote Sens.* **2022**, *14*, 792. [[CrossRef](#)]
7. Lekshmi, S.U.S.; Singh, D.N.; Baghini, M.S. A critical review of soil moisture measurement. *Measurement* **2014**, *54*, 92–105. [[CrossRef](#)]
8. Walker, J.P.; Willgoose, G.R.; Kalma, J.D. In situ measurement of soil moisture: A comparison of techniques. *J. Hydrol.* **2004**, *293*, 85–99. [[CrossRef](#)]
9. Nocita, M.; Stevens, A.; Noon, C.; van Wesemael, B. Prediction of soil organic carbon for different levels of soil moisture using Vis-NIR spectroscopy. *Geoderma* **2013**, *199*, 37–42. [[CrossRef](#)]
10. Surya, S.G.; Yuvaraja, S.; Varrla, E.; Baghini, M.S.; Palaparthi, V.S.; Salama, K.N. An in-field integrated capacitive sensor for rapid detection and quantification of soil moisture. *Sens. Actuators B Chem.* **2020**, *321*, 128542. [[CrossRef](#)]

11. Arsoy, S.; Ozgur, M.; Keskin, E.; Yilmaz, C. Usability of calcium carbide gas pressure method in hydrological sciences. *J. Hydrol.* **2013**, *503*, 67–76. [[CrossRef](#)]
12. Wang, H.; Gao, S.X.; Yue, X.Y.; Cheng, X.; Liu, Q.; Min, R.; Qu, H.; Hu, X.H. Humidity-Sensitive PMMA Fiber Bragg Grating Sensor Probe for Soil Temperature and Moisture Measurement Based on Its Intrinsic Water Affinity. *Sensors* **2021**, *21*, 6946. [[CrossRef](#)] [[PubMed](#)]
13. Li, T.; Mu, T.; Liu, G.; Yang, X.; Zhu, G.; Shang, C. A Method of Soil Moisture Content Estimation at Various Soil Organic Matter Conditions Based on Soil Reflectance. *Remote Sens.* **2022**, *14*, 2411. [[CrossRef](#)]
14. Zakeri, F.; Mariethoz, G. A review of geostatistical simulation models applied to satellite remote sensing: Methods and applications. *Remote Sens. Environ.* **2021**, *259*, 112381. [[CrossRef](#)]
15. Ahmad, U.; Alvino, A.; Marino, S. A Review of Crop Water Stress Assessment Using Remote Sensing. *Remote Sens.* **2021**, *13*, 4155. [[CrossRef](#)]
16. Yue, J.B.; Tian, J.; Tian, Q.J.; Xu, K.J.; Xu, N.X. Development of soil moisture indices from differences in water absorption between shortwave-infrared bands. *ISPRS J. Photogramm. Remote Sens.* **2019**, *154*, 216–230. [[CrossRef](#)]
17. Zhang, J.Y.; Zhang, Q.L.; Bao, A.M.; Wang, Y.J. A New Remote Sensing Dryness Index Based on the Near-Infrared and Red Spectral Space. *Remote Sens.* **2019**, *11*, 456. [[CrossRef](#)]
18. Adab, H.; Morbidelli, R.; Saltalippi, C.; Moradian, M.; Ghalhari, G.A.F. Machine Learning to Estimate Surface Soil Moisture from Remote Sensing Data. *Water* **2020**, *12*, 3223. [[CrossRef](#)]
19. Lakhankar, T.; Ghedira, H.; Temimi, M.; Sengupta, M.; Khanbilvardi, R.; Blake, R. Non-parametric Methods for Soil Moisture Retrieval from Satellite Remote Sensing Data. *Remote Sens.* **2009**, *1*, 3–21. [[CrossRef](#)]
20. Kaleita, A.L.; Tian, L.F.; Hirschi, M.C. Relationship between soil moisture content and soil surface reflectance. *Trans. ASAE* **2005**, *48*, 1979–1986. [[CrossRef](#)]
21. Zhang, D.J.; Zhou, G.Q. Estimation of Soil Moisture from Optical and Thermal Remote Sensing: A Review. *Sensors* **2016**, *16*, 1308. [[CrossRef](#)] [[PubMed](#)]
22. Zhang, R.H.; Su, H.B.; Li, Z.L.; Sun, X.M.; Tang, X.Z.; Becker, F. The potential information in the temperature difference between shadow and sunlit of surfaces and a new way of retrieving the soil moisture. *Sci. China Ser. D-Earth Sci.* **2001**, *44*, 112–123.
23. Shafian, S.; Maas, S.J. Index of Soil Moisture Using Raw Landsat Image Digital Count Data in Texas High Plains. *Remote Sens.* **2015**, *7*, 2352–2372. [[CrossRef](#)]
24. Przeździecki, K.; Zawadzki, J. Modification of the Land Surface Temperature–Vegetation Index Triangle Method for soil moisture condition estimation by using SYNOP reports. *Ecol. Indic.* **2020**, *119*, 106823. [[CrossRef](#)]
25. Khanal, S.; Fulton, J.; Shearer, S. An overview of current and potential applications of thermal remote sensing in precision agriculture. *Comput. Electron. Agric.* **2017**, *139*, 22–32. [[CrossRef](#)]
26. Huang, S.; Ding, J.; Zou, J.; Liu, B.; Zhang, J.; Chen, W. Soil moisture retrieval based on sentinel-1 imagery under sparse vegetation coverage. *Sensors* **2019**, *19*, 589. [[CrossRef](#)]
27. Shi, J.C.; Du, Y.; Du, J.Y.; Jiang, L.M.; Chai, L.N.; Mao, K.B.; Xu, P.; Ni, W.J.; Xiong, C.; Liu, Q.; et al. Progresses on microwave remote sensing of land surface parameters. *Sci. China-Earth Sci.* **2012**, *55*, 1052–1078. [[CrossRef](#)]
28. Pauwels, V.R.N.; Balenzano, A.; Satalino, G.; Skriver, H.; Verhoest, N.E.C.; Mattia, F. Optimization of Soil Hydraulic Model Parameters Using Synthetic Aperture Radar Data: An Integrated Multidisciplinary Approach. *IEEE Trans. Geosci. Remote Sens.* **2009**, *47*, 455–467. [[CrossRef](#)]
29. Hirschi, M.; Mueller, B.; Dorigo, W.; Seneviratne, S.I. Using remotely sensed soil moisture for land-atmosphere coupling diagnostics: The role of surface vs. root-zone soil moisture variability. *Remote Sens. Environ.* **2014**, *154*, 246–252. [[CrossRef](#)]
30. Yueh, S.; Shah, R.; Xu, X.; Elder, K.; Starr, B. Experimental demonstration of soil moisture remote sensing using P-band satellite signals of opportunity. *IEEE Geosci. Remote Sens. Lett.* **2019**, *17*, 207–211. [[CrossRef](#)]
31. Etminan, A.; Tabatabaenejad, A.; Moghaddam, M. Retrieving Root-Zone Soil Moisture Profile From P-Band Radar via Hybrid Global and Local Optimization. *IEEE Trans. Geosci. Remote Sens.* **2020**, *58*, 5400–5408. [[CrossRef](#)]
32. Kim, S.B.; Moghaddam, M.; Tsang, L.; Burgin, M.; Xu, X.; Njoku, E.G. Models of L-Band Radar Backscattering Coefficients Over Global Terrain for Soil Moisture Retrieval. *IEEE Trans. Geosci. Remote Sens.* **2014**, *52*, 1381–1396. [[CrossRef](#)]
33. Kim, S.; Liao, T. Towards Global Retrieval of Field-Scale Surface Soil Moisture Using L-Band Sar Data. In Proceedings of the IGARSS 2022–2022 IEEE International Geoscience and Remote Sensing Symposium, Kuala Lumpur, Malaysia, 17–22 July 2022; pp. 5452–5455.
34. Wang, H.; Magagi, R.; Goita, K. Potential of a two-component polarimetric decomposition at C-band for soil moisture retrieval over agricultural fields. *Remote Sens. Environ.* **2018**, *217*, 38–51. [[CrossRef](#)]
35. Santi, E.; Daboor, M.; Pettinato, S.; Paloscia, S. Combining Machine Learning and Compact Polarimetry for Estimating Soil Moisture from C-Band SAR Data. *Remote Sens.* **2019**, *11*, 2451. [[CrossRef](#)]
36. Karthikeyan, L.; Pan, M.; Konings, A.G.; Piles, M.; Fernandez-Moran, R.; Nagesh Kumar, D.; Wood, E.F. Simultaneous retrieval of global scale Vegetation Optical Depth, surface roughness, and soil moisture using X-band AMSR-E observations. *Remote Sens. Environ.* **2019**, *234*, 111473. [[CrossRef](#)]
37. El Hajj, M.; Baghdadi, N.; Zribi, M.; Belaud, G.; Cheviron, B.; Courault, D.; Charron, F. Soil moisture retrieval over irrigated grassland using X-band SAR data. *Remote Sens. Environ.* **2016**, *176*, 202–218. [[CrossRef](#)]

38. Liu, Y.Y.; Dorigo, W.A.; Parinussa, R.M.; de Jeu, R.A.M.; Wagner, W.; McCabe, M.F.; Evans, J.P.; van Dijk, A. Trend-preserving blending of passive and active microwave soil moisture retrievals. *Remote Sens. Environ.* **2012**, *123*, 280–297. [[CrossRef](#)]
39. Senyurek, V.; Lei, F.N.; Boyd, D.; Kurum, M.; Gurbuz, A.C.; Moorhead, R. Machine Learning-Based CYGNSS Soil Moisture Estimates over ISMN sites in CONUS. *Remote Sens.* **2020**, *12*, 1168. [[CrossRef](#)]
40. Ye, N.; Walker, J.P.; Wu, X.; Jeu, R.D.; Gao, Y.; Jackson, T.J.; Jonard, F.; Kim, E.; Merlin, O.; Pauwels, V.R.N.; et al. The Soil Moisture Active Passive Experiments: Validation of the SMAP Products in Australia. *IEEE Trans. Geosci. Remote Sens.* **2021**, *59*, 2922–2939. [[CrossRef](#)]
41. Zhao, T.; Shi, J.; Lv, L.; Xu, H.; Chen, D.; Cui, Q.; Jackson, T.J.; Yan, G.; Jia, L.; Chen, L.; et al. Soil moisture experiment in the Luan River supporting new satellite mission opportunities. *Remote Sens. Environ.* **2020**, *240*, 111680. [[CrossRef](#)]
42. Chen, Y.; Feng, X.; Fu, B. An improved global remote-sensing-based surface soil moisture (RSSM) dataset covering 2003–2018. *Earth Syst. Sci. Data* **2021**, *13*, 1–31. [[CrossRef](#)]
43. Wang, Z.; Che, T.; Zhao, T.; Dai, L.; Li, X.; Wigneron, J.P. Evaluation of SMAP, SMOS, and AMSR2 Soil Moisture Products Based on Distributed Ground Observation Network in Cold and Arid Regions of China. *IEEE J. Sel. Top. Appl. Earth Obs. Remote Sens.* **2021**, *14*, 8955–8970. [[CrossRef](#)]
44. Li, Z.-L.; Leng, P.; Zhou, C.; Chen, K.-S.; Zhou, F.-C.; Shang, G.-F. Soil moisture retrieval from remote sensing measurements: Current knowledge and directions for the future. *Earth-Sci. Rev.* **2021**, *218*, 103673. [[CrossRef](#)]
45. Yang, Y.Q.; Zhang, J.Y.; Bao, Z.X.; Ao, T.Q.; Wang, G.Q.; Wu, H.F.; Wang, J. Evaluation of Multi-Source Soil Moisture Datasets over Central and Eastern Agricultural Area of China Using In Situ Monitoring Network. *Remote Sens.* **2021**, *13*, 1175. [[CrossRef](#)]
46. Guo, J.; Bai, Q.Y.; Guo, W.C.; Bu, Z.D.; Zhang, W.T. Soil moisture content estimation in winter wheat planting area for multi-source sensing data using CNNR. *Comput. Electron. Agric.* **2022**, *193*, 106670. [[CrossRef](#)]
47. Han, L.R.; Wang, C.M.; Liu, Q.Y.; Wang, G.K.; Yu, T.; Gu, X.F.; Zhang, Y.Z. Soil Moisture Mapping Based on Multi-Source Fusion of Optical, Near-Infrared, Thermal Infrared, and Digital Elevation Model Data via the Bayesian Maximum Entropy Framework. *Remote Sens.* **2020**, *12*, 3916. [[CrossRef](#)]
48. Wang, Q.; Li, J.C.; Jin, T.Y.; Chang, X.; Zhu, Y.C.; Li, Y.W.; Sun, J.J.; Li, D.W. Comparative Analysis of Landsat-8, Sentinel-2, and GF-1 Data for Retrieving Soil Moisture over Wheat Farmlands. *Remote Sens.* **2020**, *12*, 2708. [[CrossRef](#)]
49. Han, B.; Ding, C.; Zhong, L.; Liu, J.; Qiu, X.; Hu, Y.; Lei, B. The GF-3 SAR Data Processor. *Sensors* **2018**, *18*, 835. [[CrossRef](#)]
50. Sun, J.; Yu, W.; Deng, Y. The SAR Payload Design and Performance for the GF-3 Mission. *Sensors* **2017**, *17*, 2419. [[CrossRef](#)]
51. Huang, S.; Tang, L.N.; Hupy, J.P.; Wang, Y.; Shao, G.F. A commentary review on the use of normalized difference vegetation index (NDVI) in the era of popular remote sensing. *J. For. Res.* **2021**, *32*, 1–6. [[CrossRef](#)]
52. Eroglu, O.; Kurum, M.; Boyd, D.; Gurbuz, A.C. High Spatio-Temporal Resolution CYGNSS Soil Moisture Estimates Using Artificial Neural Networks. *Remote Sens.* **2019**, *11*, 2272. [[CrossRef](#)]
53. Liu, X.; Zhu, X.; Zhang, Q.; Yang, T.; Pan, Y.; Sun, P. A remote sensing and artificial neural network-based integrated agricultural drought index: Index development and applications. *Catena* **2020**, *186*, 104394. [[CrossRef](#)]
54. Murphy, J.M.; Maggioni, M. Unsupervised Clustering and Active Learning of Hyperspectral Images with Nonlinear Diffusion. *IEEE Trans. Geosci. Remote Sens.* **2019**, *57*, 1829–1845. [[CrossRef](#)]
55. Zhang, L.P.; Wu, K.; Zhong, Y.F.; Li, P.X. A new sub-pixel mapping algorithm based on a BP neural network with an observation model. *Neurocomputing* **2008**, *71*, 2046–2054. [[CrossRef](#)]
56. Li, L.Y.; Chen, Y.; Xu, T.B.; Liu, R.; Shi, K.F.; Huang, C. Super-resolution mapping of wetland inundation from remote sensing imagery based on integration of back-propagation neural network and genetic algorithm. *Remote Sens. Environ.* **2015**, *164*, 142–154. [[CrossRef](#)]
57. Yang, X.; Liu, Y.; Wu, Z.; Yu, Y.; Li, F.; Fan, W. Forest age mapping based on multiple-resource remote sensing data. *Environ. Monit. Assess.* **2020**, *192*, 734. [[CrossRef](#)]
58. Zhan, T.; Gong, M.G.; Liu, J.; Zhang, P.Z. Iterative feature mapping network for detecting multiple changes in multi-source remote sensing images. *ISPRS J. Photogramm. Remote Sens.* **2018**, *146*, 38–51. [[CrossRef](#)]
59. Yang, X.; Yu, Y. Remote sensing inversion of soil moisture based on laboratory reflectance spectral data. *Trans. Chin. Soc. Agric. Eng.* **2017**, *33*, 195–199. [[CrossRef](#)]
60. Liu, W.D.; Baret, F.; Gu, X.F.; Tong, Q.X.; Zheng, L.F.; Zhang, B. Relating soil surface moisture to reflectance. *Remote Sens. Environ.* **2002**, *81*, 238–246.
61. Edokossi, K.; Calabria, A.; Jin, S.; Molina, I. GNSS-Reflectometry and Remote Sensing of Soil Moisture: A Review of Measurement Techniques, Methods, and Applications. *Remote Sens.* **2020**, *12*, 614. [[CrossRef](#)]
62. Yang, X.; Yu, Y. Estimating soil salinity under various moisture conditions: An experimental study. *IEEE Trans. Geosci. Remote Sens.* **2017**, *55*, 2525–2533. [[CrossRef](#)]
63. Yin, Z.; Lei, T.W.; Yan, Q.H.; Chen, Z.P.; Dong, Y.Q. A near-infrared reflectance sensor for soil surface moisture measurement. *Comput. Electron. Agric.* **2013**, *99*, 101–107. [[CrossRef](#)]
64. Yang, X.; Yu, Y.; Li, M. Estimating soil moisture content using laboratory spectral data. *J. For. Res.* **2019**, *30*, 1073–1080. [[CrossRef](#)]
65. Tian, J.; Yue, J.B.; Philpot, W.D.; Dong, X.Y.; Tian, Q.J. Soil moisture content estimate with drying process segmentation using shortwave infrared bands. *Remote Sens. Environ.* **2021**, *263*, 112552. [[CrossRef](#)]
66. Chen, W.J.; Huang, C.L.; Yang, Z.L. More severe drought detected by the assimilation of brightness temperature and terrestrial water storage anomalies in Texas during 2010–2013. *J. Hydrol.* **2021**, *603*, 126802. [[CrossRef](#)]

67. Beck, H.E.; Vergopolan, N.; Pan, M.; Levizzani, V.; van Dijk, A.; Weedon, G.P.; Brocca, L.; Pappenberger, F.; Huffman, G.J.; Wood, E.F. Global-scale evaluation of 22 precipitation datasets using gauge observations and hydrological modeling. *Hydrol. Earth Syst. Sci.* **2017**, *21*, 6201–6217. [[CrossRef](#)]
68. Xi, H.P.; Wang, S.J.; Bai, X.Y.; Tang, H.; Luo, G.J.; Li, H.W.; Wu, L.H.; Li, C.J.; Chen, H.; Ran, C.; et al. The responses of weathering carbon sink to eco-hydrological processes in global rocks. *Sci. Total Environ.* **2021**, *788*, 147706. [[CrossRef](#)]
69. Bao, Y.; Lin, L.; Wu, S.; Kwal Deng, K.A.; Petropoulos, G.P. Surface soil moisture retrievals over partially vegetated areas from the synergy of Sentinel-1 and Landsat 8 data using a modified water-cloud model. *Int. J. Appl. Earth Obs. Geoinf.* **2018**, *72*, 76–85. [[CrossRef](#)]
70. Sánchez, N.; Piles, M.; Martínez-Fernández, J.; Vall-llossera, M.; Pipia, L.; Camps, A.; Aguasca, A.; Pérez-Aragüés, F.; Herrero-Jiménez, C.M. Hyperspectral optical, thermal, and microwave L-Band observations for soil moisture retrieval at very high spatial resolution. *Photogramm. Eng. Remote Sens.* **2014**, *80*, 745–755. [[CrossRef](#)]
71. Zhou, J.H.; Crow, W.T.; Wu, Z.Y.; Dong, J.Z.; He, H.; Feng, H.H. A triple collocation-based 2D soil moisture merging methodology considering spatial and temporal non-stationary errors. *Remote Sens. Environ.* **2021**, *263*. [[CrossRef](#)]
72. Zhang, Z.; Li, Z.Y.; Chen, Y.; Zhang, L.Y.; Tao, F.L. Improving regional wheat yields estimations by multi-step-assimilating of a crop model with multi-source data. *Agric. For. Meteorol.* **2020**, *290*, 107993. [[CrossRef](#)]
73. Wang, Z.D.; Guo, P.; Wan, H.; Tian, F.Y.; Wang, L.J. Integration of Microwave and Optical/Infrared Derived Datasets from Multi-Satellite Products for Drought Monitoring. *Water* **2020**, *12*, 1504. [[CrossRef](#)]
74. Shen, R.P.; Huang, A.Q.; Li, B.L.; Guo, J. Construction of a drought monitoring model using deep learning based on multi-source remote sensing data. *Int. J. Appl. Earth Obs. Geoinf.* **2019**, *79*, 48–57. [[CrossRef](#)]
75. Smith, W.K.; Dannenberg, M.P.; Yan, D.; Herrmann, S.; Barnes, M.L.; Barron-Gafford, G.A.; Biederman, J.A.; Ferrenberg, S.; Fox, A.M.; Hudson, A.; et al. Remote sensing of dryland ecosystem structure and function: Progress, challenges, and opportunities. *Remote Sens. Environ.* **2019**, *233*, 111401. [[CrossRef](#)]
76. Crow, W.T.; Berg, A.A.; Cosh, M.H.; Loew, A.; Mohanty, B.P.; Panciera, R.; de Rosnay, P.; Ryu, D.; Walker, J.P. Upscaling sparse ground-based soil moisture observations for the validation of coarse-resolution satellite soil moisture products. *Rev. Geophys.* **2012**, *50*, RG20022. [[CrossRef](#)]
77. Tsang, L.; Ding, K.H.; Huang, S.W.; Xu, X.L. Electromagnetic Computation in Scattering of Electromagnetic Waves by Random Rough Surface and Dense Media in Microwave Remote Sensing of Land Surfaces. *Proc. IEEE* **2013**, *101*, 255–279. [[CrossRef](#)]
78. Zwieback, S.; Berg, A.A. Fine-scale SAR soil moisture estimation in the subarctic tundra. *IEEE Trans. Geosci. Remote Sens.* **2019**, *57*, 4898–4912. [[CrossRef](#)]
79. Zhang, L.; Meng, Q.; Zeng, J.; Wei, X.; Shi, H. Evaluation of Gaofen-3 C-band SAR for soil moisture retrieval using different polarimetric decomposition models. *IEEE J. Sel. Top. Appl. Earth Obs. Remote Sens.* **2021**, *14*, 5707–5719. [[CrossRef](#)]
80. Peng, J.; Albergel, C.; Balenzano, A.; Brocca, L.; Cartus, O.; Cosh, M.H.; Crow, W.T.; Dabrowska-Zielinska, K.; Dadson, S.; Davidson, M.W.J.; et al. A roadmap for high-resolution satellite soil moisture applications—Confronting product characteristics with user requirements. *Remote Sens. Environ.* **2021**, *252*, 112162. [[CrossRef](#)]
81. Zhang, L.; Lv, X.; Chen, Q.; Sun, G.; Yao, J. Estimation of surface soil moisture during corn growth stage from SAR and optical data using a combined scattering model. *Remote Sens.* **2020**, *12*, 1844. [[CrossRef](#)]
82. Peng, J.; Loew, A.; Merlin, O.; Verhoest, N.E.C. A review of spatial downscaling of satellite remotely sensed soil moisture. *Rev. Geophys.* **2017**, *55*, 341–366. [[CrossRef](#)]
83. Qiu, J.; Crow, W.T.; Wagner, W.; Zhao, T. Effect of vegetation index choice on soil moisture retrievals via the synergistic use of synthetic aperture radar and optical remote sensing. *Int. J. Appl. Earth Obs. Geoinf.* **2019**, *80*, 47–57. [[CrossRef](#)]
84. Sobrino, J.A.; Franch, B.; Mattar, C.; Jiménez-Muñoz, J.C.; Corbari, C. A method to estimate soil moisture from Airborne Hyperspectral Scanner (AHS) and ASTER data: Application to SEN2FLEX and SEN3EXP campaigns. *Remote Sens. Environ.* **2012**, *117*, 415–428. [[CrossRef](#)]
85. Anderson, M.C.; Yang, Y.; Xue, J.; Knipper, K.R.; Yang, Y.; Gao, F.; Hain, C.R.; Kustas, W.P.; Cawse-Nicholson, K.; Hulley, G.; et al. Interoperability of ECOSTRESS and Landsat for mapping evapotranspiration time series at sub-field scales. *Remote Sens. Environ.* **2021**, *252*, 112189. [[CrossRef](#)]
86. Martens, B.; Miralles, D.G.; Lievens, H.; van der Schalie, R.; de Jeu, R.A.M.; Fernandez-Prieto, D.; Beck, H.E.; Dorigo, W.A.; Verhoest, N.E.C. GLEAM v3: Satellite-based land evaporation and root-zone soil moisture. *Geosci. Model Dev.* **2017**, *10*, 1903–1925. [[CrossRef](#)]
87. Gruber, A.; de Lannoy, G.; Albergel, C.; Al-Yaari, A.; Brocca, L.; Calvet, J.C.; Colliander, A.; Cosh, M.; Crow, W.; Dorigo, W.; et al. Validation practices for satellite soil moisture retrievals: What are (the) errors? *Remote Sens. Environ.* **2020**, *244*, 111806. [[CrossRef](#)]
88. Lee, J.H.; Zhao, C.F.; Kerr, Y. Stochastic Bias Correction and Uncertainty Estimation of Satellite-Retrieved Soil Moisture Products. *Remote Sens.* **2017**, *9*, 847. [[CrossRef](#)]
89. Li, C.M.; Tang, G.Q.; Hong, Y. Cross-evaluation of ground-based, multi-satellite and reanalysis precipitation products: Applicability of the Triple Collocation method across Mainland China. *J. Hydrol.* **2018**, *562*, 71–83. [[CrossRef](#)]
90. Zhang, L.; Wang, F.; Xu, B.; Chi, W.; Wang, Q.; Sun, T. Prediction of stock prices based on LM-BP neural network and the estimation of overfitting point by RDCI. *Neural Comput. Appl.* **2018**, *30*, 1425–1444. [[CrossRef](#)]
91. Ali, I.; Greifeneder, F.; Stamenkovic, J.; Neumann, M.; Notarnicola, C. Review of Machine Learning Approaches for Biomass and Soil Moisture Retrievals from Remote Sensing Data. *Remote Sens.* **2015**, *7*, 16398–16421. [[CrossRef](#)]

92. Mas, J.F.; Flores, J.J. The application of artificial neural networks to the analysis of remotely sensed data. *Int. J. Remote Sens.* **2008**, *29*, 617–663. [[CrossRef](#)]
93. Wu, W.; Clark, J.S.; Vose, J.M. Assimilating multi-source uncertainties of a parsimonious conceptual hydrological model using hierarchical Bayesian modeling. *J. Hydrol.* **2010**, *394*, 436–446. [[CrossRef](#)]
94. Grunwald, S.; Vasques, G.M.; Rivero, R.G. Fusion of Soil and Remote Sensing Data to Model Soil Properties. In *Advances in Agronomy*; Sparks, D.L., Ed.; Elsevier: Amsterdam, The Netherlands, 2015; Volume 131, pp. 1–109.
95. Tian, J.X.; Qin, J.; Yang, K.; Zhao, L.; Chen, Y.Y.; Lu, H.; Li, X.; Shi, J.C. Improving surface soil moisture retrievals through a novel assimilation algorithm to estimate both model and observation errors. *Remote Sens. Environ.* **2022**, *269*, 112802. [[CrossRef](#)]

Disclaimer/Publisher’s Note: The statements, opinions and data contained in all publications are solely those of the individual author(s) and contributor(s) and not of MDPI and/or the editor(s). MDPI and/or the editor(s) disclaim responsibility for any injury to people or property resulting from any ideas, methods, instructions or products referred to in the content.